INTERNATIONAL JOURNAL FOR NUMERICAL METHODS IN FLUIDS
Int. J. Numer. Meth. Fluids 2008; **58**:237–261

A second-order semi-implicit hybrid scheme for one-dimensional Boussinesq-type waves in rectangular channels

Sandra Soares-Frazão[1,*,†] and Vincent Guinot[2]

[1]*Unité de Génie Civil et Environnemental, Université catholique de Louvain, Place du Levant 1, 1348 Louvain-la-Neuve, Belgium*
[2]*Hydrosciences Montpellier UMR5569 (CNRS, IRD, UM1, UM2), Université Montpellier 2, Maison des Sciences de l'Eau, 34095 Montpellier Cedex 5, France*

SUMMARY

A numerical procedure is proposed for the solution of the Boussinesq equations in rectangular channels over a horizontal bed. The Boussinesq equations account for non-hydrostatic effects in free-surface flows. The proposed approach is a predictor–corrector procedure where the hyperbolic part of the equations is treated using a higher-order estimate of the variable slope of the Godunov-type, MUSCL scheme. The proposed slope estimate is third-order accurate on irregular grids and fourth-order accurate on regular grids. The dispersive, non-hydrostatic terms are treated using a semi-implicit discretization. A stability analysis of the proposed predictor–corrector procedure shows that optimal accuracy is achieved when the implicitation parameter is set equal to 0.5. This analysis is confirmed by numerical experiments, whereby the propagation of a solitary wave and the development of an undular bore are reproduced and compared successfully with the available analytical solutions. The proposed method is shown to be of a good level of accuracy without being too sensitive to the numerical parameters. Its applicability in practical problems is illustrated by a comparison with laboratory experiments. Copyright © 2008 John Wiley & Sons, Ltd.

Received 22 September 2006; Revised 17 October 2007; Accepted 20 October 2007

KEY WORDS: Boussinesq equations; undular bore; predictor–corrector; fourth-order slope reconstruction; stability analysis

1. INTRODUCTION

Flows in rivers and channels are commonly described using the shallow-water theory, assuming hydrostatic pressure distribution and depth-averaged velocity. In this shallow-water context, sharp transitions between two different flow states result in a discontinuity in both the water surface and the velocity. These are referred to as bores. In reality, for large transitions, such a bore takes

---

[*] Correspondence to: Sandra Soares-Frazão, Unité de Génie Civil et Environnemental, Université catholique de Louvain, Place du Levant 1, 1348 Louvain-la-Neuve, Belgium.

[†] E-mail: soares@gce.ucl.ac.be

the form of a breaking wave with turbulent rollers. However, transitions of moderate amplitude are accompanied by wave trains without any wave breaking. These are called undular bores. Such undular bores are the consequence of the weak non-hydrostaticity of the pressure distribution [1, 2]. An undular bore can also grow in shallow flows over obstacles [3], or occur as internal undular bores in the density-stratified waters of the coastal ocean [4].

The Boussinesq equations include some additional dispersive terms compared with the shallow-water equations. Such dispersive terms allow weak non-hydrostaticity to be accounted for by assuming that the vertical-velocity component varies linearly from the bottom to the free surface. These equations can be used to represent solitary wave propagation or Favre waves, which are secondary undulations developing at the head of a bore for flows with a Froude number up to approximately 1.23 [2, 5]. The wave train created behind a moving front is the result of the necessity to dissipate energy. For larger Froude numbers, the energy is dissipated in a moving roller at the breaking front wave. As they are not based on an energy interpretation of the phenomenon [6], the Boussinesq equations do not account for the breaking of the waves. On the contrary, they cause the amplitude of the undulations to grow with increasing Froude numbers.

The analytical study conducted in [7] allowed unsteady undular bores to be described in the fully nonlinear theory, and showed how bores remain unsteady and their amplitude grows in time in the absence of any dissipation in the equations. A numerical solution to the Boussinesq equations is thus to be found in their range of validity, namely gradually varied flows, solitary waves where a permanent shape solution is sought and cnoidal wave trains where a periodical solution is sought [8].

Besides the pioneering experimental work of Favre [3], other authors have conducted laboratory or field measurements of such undular bores. Among them, Benet and Cunge [9] and Treske [10] have investigated surge waves in trapezoidal channels, Ponsy and Carbonnell [11] have conducted a photogrammetry investigation and Marche *et al.* [12] have observed such waves in dam-break-induced flows.

Several finite-difference schemes have been developed to solve the complete set of Boussinesq equations [2, 13–15] in order to compute the development of an undular bore, generally starting from a smooth initial water profile. The scheme by Prüser and Zielke [14] was compared with experiments: good agreement was obtained for the water depth, but the wave propagation speed was inaccurate. Bratsos *et al.* [16] developed a parametric finite-difference model, investigating the influence of the implicitation parameter, and comparing the results with those obtained with a commercial modelling package.

A hybrid finite-volume approach was developed in [1] that allowed for steep flow gradients as initial conditions, but showed some numerical diffusion of the results when compared with experiments. Such an approach was adopted and extended to higher-order accuracy in [17, 18]. Higher-order accuracy was also achieved in [19], where the detailed stability analysis of a finite-volume scheme is presented. This latter scheme was successfully used to simulate the propagation of a solitary wave. A second-order model developed by Stansby [20], as in [19], does not use Riemann solvers to compute the intercell fluxes.

Finite-element methods were also developed to solve the Boussinesq equations [21, 22] and compared with experimental data. A finite-element discretization with a weighted residual technique for the solution approach within each element is presented by Antunes Do Carmo *et al.* [23] and compared with experimental data. Then, the semi-implicit method by Walters [24] yields a robust scheme, used to simulate tsunami wave propagation, although it is quite diffusive when compared with the analytical solution of a solitary wave.

Besides, many developments were conducted on simplified forms of the Boussinesq equations. The Korteweg–de-Vries equation (KdV [25]) and the regularized long-wave (RLW) equation (see, e.g. [26, 27]) are uni-directional forms of the Boussinesq equations, where the convective terms are neglected. Therefore, while the Boussinesq equations consist of a continuity and momentum equation, the KdV and RLW equations are scalar equations describing the evolution of the water elevation only. Sanders *et al.* [28] investigated the properties of unidirectional and bidirectional equations by means of a Fourier pseudospectral method.

The present paper focuses on the solution of the Boussinesq equations for rectangular channels with a horizontal bed. An improved discretization of the hyperbolic term is provided, and a new discretization method for the dispersion term is introduced. This formulation is less sensitive to the computational time step than previous work presented in [1]. The approach is first validated by comparison with the analytical solution of a solitary wave. Then, a comparison with an experimental test case illustrates the usefulness of the Boussinesq equations when non-hydrostatic terms cannot be neglected in the momentum equation.

2. GOVERNING EQUATIONS AND SOLUTION PROPERTIES

The Boussinesq equations read (see [1] for the details of the derivation)

$$\begin{gathered}\frac{\partial h}{\partial t}+\frac{\partial q}{\partial x}=0\\ \frac{\partial q}{\partial t}+\frac{\partial}{\partial x}\left(\frac{q^2}{h}+g\frac{h^2}{2}\right)-\frac{h^2}{3}\left[\frac{\partial^3 q}{\partial t\,\partial x^2}-u\frac{\partial^3 h}{\partial t\,\partial x^2}+u\frac{\partial^3 q}{\partial x^3}-u^2\frac{\partial^3 h}{\partial x^3}\right]=gh(S_0-S_{\mathrm{f}})\end{gathered}\tag{1}$$

where h is the water depth, g is the gravitational acceleration, $q=hu$ is the unit discharge, u being the depth-averaged flow velocity and S_0 and S_{f} are the bottom and energy slopes, respectively. S_{f} is classically accounted for by a Manning–Strickler friction law

$$S_{\mathrm{f}}=\frac{|u|u}{K^2R_{\mathrm{H}}^{4/3}}=\frac{n^2|u|u}{R_{\mathrm{H}}^{4/3}}\tag{2}$$

where K and n are Strickler's and Manning's friction coefficients, respectively, and R_{H} is the hydraulic radius of the channel, that is, the ratio of the cross-sectional area of the channel to the wetted perimeter. In the case of a rectangular channel of width b as dealt with in the present paper, R_{H} is given by

$$R_{\mathrm{H}}=\frac{bh}{b+2h}\approx h\quad\text{if } h\ll b\tag{3}$$

Equations (1) can be expressed in vector conservation form as

$$\frac{\partial \mathbf{U}}{\partial t}+\frac{\partial \mathbf{F}}{\partial x}-\mathbf{D}\left(\frac{\partial^3\mathbf{U}}{\partial t\partial x^2}+u\frac{\partial^3\mathbf{U}}{\partial x^3}\right)=\mathbf{S}\tag{4}$$

where the conserved variable $\mathbf{U}$, the flux $\mathbf{F}$, the dispersion matrix $\mathbf{D}$ and the source term $\mathbf{S}$ are defined as

$$\begin{gathered}\mathbf{U}=\begin{bmatrix}h\\ q\end{bmatrix},\quad \mathbf{F}=\begin{bmatrix}q\\ \sigma\end{bmatrix}=\begin{bmatrix}q\\ q^2/h+gh^2/2\end{bmatrix}\\ \mathbf{D}=\frac{h^2}{3}\begin{bmatrix}0 & 0\\ -u & 1\end{bmatrix},\quad \mathbf{S}=\begin{bmatrix}0\\ (S_0-S_\mathrm{f})gh\end{bmatrix}\end{gathered}\tag{5}$$

Note that Equation (4) can also be rewritten in non-conservative form as

$$\frac{\partial\mathbf{U}}{\partial t}+\mathbf{A}\frac{\partial\mathbf{U}}{\partial x}=\mathbf{D}\left(\frac{\partial^3\mathbf{U}}{\partial t\partial x^2}+u\frac{\partial^3\mathbf{U}}{\partial x^3}\right)+\mathbf{S}=\mathbf{H}+\mathbf{S}\tag{6}$$

where $\mathbf{H}$ is the matrix related to the dispersive terms $\mathbf{H}=\mathbf{D}(\partial^3\mathbf{U}/\partial t\partial x^2+u\partial^3\mathbf{U}/\partial x^3)$ and $\mathbf{A}$ is the Jacobian matrix $\mathbf{A}=\partial\mathbf{F}/\partial\mathbf{U}$ given by

$$\mathbf{A}=\begin{bmatrix}0 & 1\\ c^2-u^2 & 2u\end{bmatrix}\tag{7}$$

where $c=(gh)^{1/2}$ is the propagation speed of pressure waves in still water in the shallow-water theory.

The behaviour of the analytical solution is analysed under the assumption of frictionless motion in a horizontal channel. A harmonic analysis is carried out by linearizing Equation (6) around a uniform, reference flow state (h_0, q_0). The resulting perturbation equation is

$$\frac{\partial\mathbf{V}}{\partial t}+\mathbf{A}_0\frac{\partial\mathbf{V}}{\partial x}-\mathbf{D}_0\left(\frac{\partial^3\mathbf{V}}{\partial t\partial x^2}+u_0\frac{\partial^3\mathbf{V}}{\partial x^3}\right)=0\tag{8}$$

where $\mathbf{V}=[h-h_0, q-q_0]^\mathrm{T}$ is the vector of the flow perturbation from the uniform state and the subscript 0 indicates that the values of $\mathbf{A}$, $\mathbf{D}$ and u are taken for the reference state (h_0, q_0). The solutions of Equation (8) are sought in the form

$$\mathbf{V}(x,t)=\mathbf{V}_0\exp(\omega t+\mathrm{j}\mu x)\tag{9}$$

where j is the pure imaginary number such that $\mathrm{j}^2=-1$, the space pulsation μ is a pure real number and the time pulsation ω is to be determined for a given μ. Solution (9) of Equation (8) is stable if the real part of ω is negative. From the predefined form (9), it follows that

$$\frac{\partial^{p+k}\mathbf{V}}{\partial t^p\partial x^k}=\omega^p(\mathrm{j}\mu)^k\mathbf{V}\tag{10}$$

Substituting Equation (10) into Equation (8) yields an equation of the type

$$\mathbf{MV}=0\tag{11}$$

with the matrix $\mathbf{M}$ given by

$$\mathbf{M}=\omega\mathbf{I}+\mathrm{j}\mu\mathbf{A}_0+(\omega\mu^2+\mathrm{j}u_0\mu^3)\mathbf{D}_0\tag{12}$$

where **I** is the 2×2 identity matrix. Equation (11) has non-trivial solutions only if the determinant of **M** is zero, that is

$$\begin{vmatrix} \omega & \mathrm{j}\mu \\ -ku_0\omega+[c_0^2-(1+k)u_0^2]\mathrm{j}\mu & (1+k)\omega+\mathrm{j}(2+k)u_0\mu \end{vmatrix}=0 \tag{13}$$

where the dimensionless number k is defined as

$$k=\tfrac{1}{3}(h_0\mu)^2 \tag{14}$$

Solving Equation (13) for ω yields

$$\omega=-\left[u_0\pm\frac{c_0}{(1+k)^{1/2}}\right]\mathrm{j}\mu \tag{15}$$

Note that ω has a zero real part, which means that the solution is neither amplified nor damped. It may, however, be subject to deformation in time due to a possible dependence of the propagation speed of the waves on the wavelength. Equation (15) allows the phase velocity (also called celerity) of the waves to be determined. The phase velocity, denoted by λ hereafter, verifies the condition

$$\mathbf{V}(x,t)=\mathbf{V}(x-\lambda t,0) \tag{16}$$

Substituting Equation (9) into Equation (16) yields

$$\lambda=\frac{\mathrm{j}\omega}{\mu} \tag{17}$$

Substituting Equation (15) into Equation (17) leads to the final expressions for λ

$$\begin{aligned} \lambda^{(1)}&=u_0-(1+k)^{-1/2}c_0 \\ \lambda^{(2)}&=u_0+(1+k)^{-1/2}c_0 \end{aligned} \tag{18}$$

As in the shallow-water theory the solution of Equation (1) is the sum of two solutions propagating at two different phase velocities $\lambda^{(1)}$ and $\lambda^{(2)}$, and the phase velocities are equal to the sum of the local flow velocity and the propagation speed of the waves in still water (in the direction of negative x and in the direction of positive x). In contrast with the shallow-water theory, the propagation speed of the waves in still water depends on the ratio between the wavelength and the water depth *via* the dimensionless number k defined in Equation (14). The space pulsation μ being related to the wavelength L by $\mu=2\pi/L$, k is a decreasing function of the ratio h_0/L. Therefore, the propagation speed of the waves in still water is an increasing function of the wavelength L. For a wave of infinite length, k tends to zero and the phase velocities λ tend to the celerities of the classical shallow-water theory. Figure 1 illustrates the behaviour of the phase speed of the waves in still water as a function of L/h_0.

The group velocity κ is defined as [29]

$$\kappa=\frac{\mathrm{d}(\lambda\mu)}{\mathrm{d}\mu} \tag{19}$$

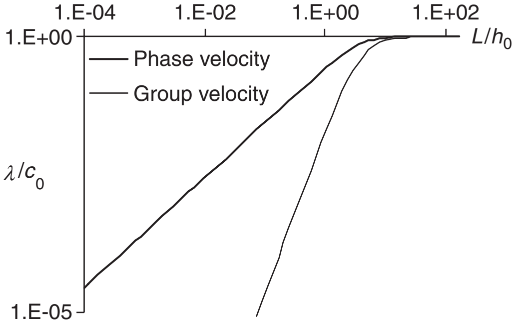

Figure 1. Phase velocity and group velocity in still water as functions of the ratio of the wavelength to the water depth. Logarithmic coordinates for both axes.

Substituting Equations (18) into (19) leads to the following expressions for the group velocities:

$$\begin{aligned}\kappa^{(1)} &= u_0 - (1+k)^{-3/2} c_0 \\ \kappa^{(2)} &= u_0 + (1+k)^{-3/2} c_0\end{aligned} \tag{20}$$

The group velocity in still water decreases faster than the phase velocity as the wavelength decreases. This behaviour is illustrated in Figure 1.

3. NUMERICAL TECHNIQUE

A shock-capturing finite-volume scheme is used to solve the hyperbolic part of the equations [30]. This allows flows with sharp discontinuities, or sharp initial conditions, to be simulated. Such flow configurations include, e.g. the sudden increase or decrease in the discharge following the instantaneous opening or closing of a gate, as illustrated in the applications. The bed slope and friction source terms are neglected from this point for the sake of clarity and simplicity of the developments. The dispersive terms are treated using a semi-implicit discretization. Eventually, various MUSCL-type variable reconstruction schemes are used, among which a new fourth-order slope estimate is presented in Section 3.3.

3.1. Outline of the approach

A finite-volume discretization [31] of the integral form of (1) applied to a mesh of the space–time computational grid of Figure 2 yields, considering the dispersive term separately as an external source term,

$$\mathbf{U}_i^{n+1} = \mathbf{U}_i^n - \frac{\Delta t}{\Delta x}(\overline{\mathbf{F}}_{i+1/2} - \overline{\mathbf{F}}_{i-1/2}) + \mathbf{H}_i \Delta t \tag{21}$$

where $\mathbf{H}_i$ denotes the results of the discrete integration of the dispersive term over the area Ω (Figure 2).

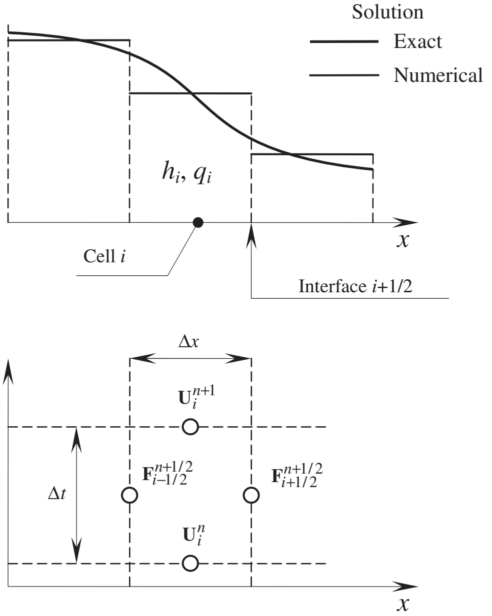

Figure 2. Definition of variables and computational grid in the physical space (top) and in the phase space (bottom).

The inter-cell fluxes $\overline{\mathbf{F}}_{i-1/2}$ and $\overline{\mathbf{F}}_{i+1/2}$ are calculated as functions of initial vectors $\mathbf{U}_i^n$ and $\mathbf{U}_{i+1}^n$, using Roe's scheme under the form [30]

$$\overline{\mathbf{F}}_{i+1/2}=\frac{1+Fr^*}{2}\mathbf{F}_i^n+\frac{1-Fr^*}{2}\mathbf{F}_{i+1}^n+c^*\frac{1-Fr^{*2}}{2}(\mathbf{U}_i^n-\mathbf{U}_{i+1}^n) \tag{22}$$

where Fr is the Froude number and the superscript $*$ denotes averaged values at the cell interfaces, calculated as

$$Fr^*=\frac{u^*}{c^*},\quad u^*=\frac{c_i u_i+c_{i+1}u_{i+1}}{c_i+c_{i+1}},\quad c^*=\sqrt{g\frac{h_i+h_{i+1}}{2}} \tag{23}$$

Limiting the absolute value of Fr to unity allows both subcritical ($Fr<1$) and supercritical ($Fr\geqslant 1$) conditions to be accounted for by Equation (22). A predictor–corrector scheme is used to account for the semi-implicit discretization of the dispersive term.

3.1.1. Predictor step. System (21) without the dispersive term $\mathbf{H}_i$ is solved explicitly to find a provisional value $\mathbf{U}_i^{\text{pred}}$ of $\mathbf{U}_i^{n+1}$. This step is expressed as

$$\mathbf{U}_i^{\text{pred}}=\mathbf{U}_i^n+\frac{\Delta t}{\Delta x}(\bar{\mathbf{F}}_{i-1/2}^{(n)}-\bar{\mathbf{F}}_{i+1/2}^{(n)}) \tag{24}$$

where $\bar{\mathbf{F}}_{i+1/2}^{(n)}$ is the numerical flux vector at the interface between cells i and $i+1$ calculated according to Equations (22)–(23), using the values $\mathbf{U}_i^n$.

3.1.2. Implicit step for the non-hydrostatic source term of the momentum equation. The momentum equation in (21) including the dispersive terms is discretized using a semi-implicit finite-difference approximation for the dispersive term. The implicitation factor θ ranges from 0 to 1. The value $\theta=1$ corresponds to a fully implicit discretization of the dispersion terms, while a fully explicit discretization is obtained for $\theta=0$

$$\begin{aligned}
q_i^{n+1} &= q_i^n - \frac{\Delta t}{\Delta x}[(1-\theta)(\bar{\sigma}_{i+1/2}^{(n)} - \bar{\sigma}_{i-1/2}^{(n)}) + \theta(\bar{\sigma}_{i+1/2}^{\text{pred}} - \bar{\sigma}_{i-1/2}^{\text{pred}})] \\
&\quad + \frac{(h_i^n)^3}{3\Delta x^2}\left(\frac{q_{i+1}^{n+1}}{h_{i+1}^{\text{pred}}} - 2\frac{q_i^{n+1}}{h_i^{\text{pred}}} + \frac{q_{i-1}^{n+1}}{h_{i-1}^{\text{pred}}} - \frac{q_{i+1}^n}{h_{i+1}^n} + 2\frac{q_i^n}{h_i^n} - \frac{q_{i-1}^n}{h_{i-1}^n}\right) \\
&\quad + (1-\theta)\left[\frac{(h_i^n)^3\Delta t}{6\Delta x^3}\frac{q_i^n}{h_i^n}\left(\frac{q_{i+2}^n}{h_{i+2}^n} - 2\frac{q_{i+1}^n}{h_{i+1}^n} + 2\frac{q_{i-1}^n}{h_{i-1}^n} - \frac{q_{i-2}^n}{h_{i-2}^n}\right)\right] \\
&\quad + \theta\left[\frac{(h_i^{\text{pred}})^3\Delta t}{6\Delta x^3}\frac{q_i^{\text{pred}}}{h_i^{\text{pred}}}\left(\frac{q_{i+2}^{n+1}}{h_{i+2}^{\text{pred}}} - 2\frac{q_{i+1}^{n+1}}{h_{i+1}^{\text{pred}}} + 2\frac{q_{i-1}^{n+1}}{h_{i-1}^{\text{pred}}} - \frac{q_{i-2}^{n+1}}{h_{i-2}^{\text{pred}}}\right)\right]
\end{aligned} \tag{25}$$

The momentum flux $\bar{\sigma}_{i+1/2}^{\text{pred}}$ is evaluated by Roe's scheme, according to (22)–(23), but with the updated variables $\mathbf{U}_i^{\text{pred}}$ issued from the predictor step (24)

$$\begin{aligned}
\bar{\sigma}_{i+1/2}^{\text{pred}} &= \frac{1+Fr^*}{2}\left[q_i^{\text{pred}} + g\frac{(h_i^{\text{pred}})^2}{2}\right] + \frac{1-Fr^*}{2}\left[q_{i+1}^{\text{pred}} + g\frac{(h_{i+1}^{\text{pred}})^2}{2}\right] \\
&\quad + c^*\frac{1-(Fr^*)^2}{2}(q_i^{\text{pred}} - q_{i+1}^{\text{pred}})
\end{aligned} \tag{26}$$

The interface-averaged Froude number Fr^* and celerity c^* are computed from (23) also using the variables $\mathbf{U}_i^{\text{pred}}$. The result of this implicit step is the updated value q_i^{n+1}.

Equation (25) can be rewritten as

$$\begin{aligned}
&\left(\theta\frac{\Delta t}{6\Delta x^3}\frac{(h_i^{\text{pred}})^2 q_i^{\text{pred}}}{h_{i-2}^{\text{pred}}}\right)q_{i-2}^{n+1} + \left(-\frac{1}{3}\frac{(h_i^n)^3}{\Delta x^2 h_{i-1}^{\text{pred}}} - \theta\frac{\Delta t}{3\Delta x^3}\frac{(h_i^{\text{pred}})^2 q_i^{\text{pred}}}{h_{i-1}^{\text{pred}}}\right)q_{i-1}^{n+1} \\
&\quad + \left(1 + \frac{2}{3}\frac{(h_i^n)^3}{\Delta x^2 h_i^{\text{pred}}}\right)q_i^{n+1} - \left(\frac{1}{3}\frac{(h_i^n)^3}{\Delta x^2 h_{i+1}^{\text{pred}}} + \theta\frac{\Delta t}{3\Delta x^3}\frac{(h_i^{\text{pred}})^2 q_i^{\text{pred}}}{h_{i+1}^{\text{pred}}}\right)q_{i+1}^{n+1} \\
&\quad + \left(-\theta\frac{\Delta t}{6\Delta x^3}\frac{(h_i^{\text{pred}})^2 q_i^{\text{pred}}}{h_{i+2}^{\text{pred}}}\right)q_{i-2}^{n+1} \\
&= \left(-(1-\theta)\frac{\Delta t}{6\Delta x^3}\frac{(h_i^n)^2 q_i^n}{h_{i-2}^n}\right)q_{i-2}^n + \left(-\frac{1}{3}\frac{(h_i^n)^3}{\Delta x^2 h_{i-1}^n} + (1-\theta)\frac{\Delta t}{3\Delta x^3}\frac{(h_i^n)^2 q_i^n}{h_{i-1}^n}\right)q_{i-1}^n
\end{aligned}$$

$$
\begin{aligned}
&+\left(1+\frac{2}{3}\frac{(h_i^n)^3}{\Delta x^2 h_i^n}\right) q_i^n + \left(-\frac{1}{3}\frac{(h_i^n)^3}{\Delta x^2 h_{i+1}^n} - (1-\theta)\frac{\Delta t}{3\Delta x^3}\frac{(h_i^n)^2 q_i^n}{h_{i+1}^n}\right) q_{i+1}^n \\
&+\left((1-\theta)\frac{\Delta t}{6\Delta x^3}\frac{(h_i^n)^2 q_i^n}{h_{i+2}^n}\right) q_{i+2}^n \\
&+\frac{\Delta t}{\Delta x}((1-\theta)(\bar{\sigma}^{(n)}_{i-1/2}-\bar{\sigma}^{(n)}_{i+1/2})+\theta(\bar{\sigma}^{\text{pred}}_{i-1/2}-\bar{\sigma}^{\text{pred}}_{i+1/2})) \qquad (27)
\end{aligned}
$$

3.1.3. Corrector step for the continuity equation. Finally, the continuity equation is solved again to find h_i^{n+1}:

$$h_i^{n+1} = h_i^n - \frac{\Delta t}{\Delta x}(\bar{q}^{\text{corr}}_{i+1/2} - \bar{q}^{\text{corr}}_{i-1/2}) \qquad (28)$$

The mass flux $\bar{q}^{\text{corr}}_{i+1/2}$ in (28) is evaluated using the average values of the mass flux q

$$\bar{q}^{\text{corr}}_{i+1/2} = \frac{1+Fr^*}{2}\frac{q_i^n+q_i^{n+1}}{2} + \frac{1-Fr^*}{2}\frac{q_{i+1}^n+q_{i+1}^{n+1}}{2} - c^*\frac{1-(Fr^*)^2}{2}(h_i^n - h_{i+1}^n) \qquad (29)$$

3.2. Hybrid finite-volume scheme solution steps

The key steps in applying the proposed hybrid scheme to find the solution $\mathbf{U}_i^{n+1}$ of Equations (1) at time t^{n+1} from the known variables $\mathbf{U}_i^n$ at time t^n are summarized here:

1. Compute the intercell fluxes for the hyperbolic part of the equations from (22).
2. Find a provisional value for $\mathbf{U}_i^{(n+1)}$, i.e. $h_i^{(n+1)}$ and $q_i^{(n+1)}$ by applying the predictor step (24).
3. Compute the effect of the dispersive terms in the momentum equation by applying the implicit step. This consists in solving the pentadiagonal matrix arising from Equation (27) to find the final value of q_i^{n+1}.
4. Apply the corrector step (29) to find the final value of h_i^{n+1}.

The pentadiagonal system of step 3 is solved by LU factorization, taking into account the limited bandwidth of the matrix.

3.3. Numerical treatment of the dispersion terms

The present subsection focuses on the numerical treatment of the dispersive part of Equation (1). The stability analysis is first carried out in the framework of the time splitting technique [32, 33], where it is assumed that the hyperbolic part of the equation has already been solved and that the only remaining problem is the solution of

$$\frac{\partial \mathbf{U}}{\partial t} - \mathbf{D}\left(\frac{\partial^3 \mathbf{U}}{\partial t \partial x^2} + u\frac{\partial^3 \mathbf{U}}{\partial x^3}\right) = 0 \qquad (30)$$

The stability analysis is extended to the proposed predictor–corrector procedure at the end of the present section. The fully time- and space-centred discretization is proposed in (25) for the derivative $\partial^3\mathbf{U}/\partial t\partial x^2$ on a regular grid

$$\frac{\partial^3\mathbf{U}}{\partial t\partial x^2}\approx\frac{1}{\Delta t}\left[\left(\frac{\partial^2\mathbf{U}}{\partial x^2}\right)^{n+1}-\left(\frac{\partial^2\mathbf{U}}{\partial x^2}\right)^{n}\right]$$

$$\approx\frac{1}{\Delta t\Delta x^2}[(\mathbf{U}_{i-1}^{n+1}-2\mathbf{U}_i^{n+1}+\mathbf{U}_{i+1}^{n+1})-(\mathbf{U}_{i-1}^{n}-2\mathbf{U}_i^{n}+\mathbf{U}_{i+1}^{n})] \tag{31}$$

while a semi-implicit discretization is proposed for the derivative $\partial^3\mathbf{U}/\partial x^3$:

$$\frac{\partial^3\mathbf{U}}{\partial x^3}\approx\theta\left(\frac{\partial^3\mathbf{U}}{\partial x^3}\right)^{n+1}+(1-\theta)\left(\frac{\partial^3\mathbf{U}}{\partial x^3}\right)^{n}$$

$$\approx\frac{1}{2\Delta x^3}[\theta(-\mathbf{U}_{i-2}^{n+1}+2\mathbf{U}_{i-1}^{n+1}-2\mathbf{U}_{i+1}^{n+1}+\mathbf{U}_{i+2}^{n+1})$$

$$+(1-\theta)(-\mathbf{U}_{i-2}^{n}+2\mathbf{U}_{i-1}^{n}-2\mathbf{U}_{i+1}^{n}+\mathbf{U}_{i+2}^{n})] \tag{32}$$

The time derivative is classically discretized as

$$\frac{\partial\mathbf{U}}{\partial t}\approx\frac{1}{\Delta t}(\mathbf{U}_i^{n+1}-\mathbf{U}_i^{n}) \tag{33}$$

and the matrix **D** is evaluated using an explicit discretization. Prior to carrying out the stability analysis, it is noted from the definition of **D** in Equation (5) that solving Equation (30) leaves the first component h of the conserved variable **U** unchanged, that is

$$h_i^{n+1}=h_i^n \tag{34}$$

Therefore, it is sufficient to carry out the stability analysis of the second component of the numerical solution of the vector equation (30) alone, that is

$$\frac{\partial q}{\partial t}-\frac{h_0^2}{3}\left(\frac{\partial^3 q}{\partial t\partial x^2}+u_0\frac{\partial^3 q}{\partial x^3}\right)=\frac{h_0^2u_0}{3}\left(\frac{\partial^3 h}{\partial t\partial x^2}+u_0\frac{\partial^3 h}{\partial x^3}\right) \tag{35}$$

where h_0 and u_0 are the reference water depth and velocity, considered as constant coefficients for the sake of the linear stability analysis. Note that third-order derivatives in h in the right-hand side of Equation (35) remain constant when solving the equation to find q_i^{n+1}, as expressed by Equation (34). Consequently, the right-hand side of Equation (35) is considered as a constant in the linear stability analysis. Therefore, the stability analysis needs to be carried out only for the homogeneous part of Equation (35), that is

$$\frac{\partial q}{\partial t}-\frac{h^2}{3}\left(\frac{\partial^3 q}{\partial t\partial x^2}+u\frac{\partial^3 q}{\partial x^3}\right)=0 \tag{36}$$

For the sake of clarity in the developments hereafter, the numerical second- and third-order differentiation operators $\mathbf{d}_2$ and $\mathbf{d}_3$ are introduced:

$$\begin{aligned} \mathbf{d}_2 q_i^n &= \frac{1}{\Delta x^2}(q_{i-1}^n - 2q_i^n + q_{i+1}^n) \\ \mathbf{d}_3 q_i^n &= \frac{1}{2\Delta x^3}(-q_{i-1}^n + 2q_{i-1}^n - 2q_{i+1}^n + q_{i+2}^n) \end{aligned} \tag{37}$$

Using these definitions the second components of Equations (31)–(33) can be rewritten as

$$\begin{aligned} \frac{\partial q}{\partial t} &\approx \frac{1}{\Delta t}(q_i^{n+1} - q_i^n) \\ \frac{\partial^3 q}{\partial t \partial x^2} &\approx \frac{1}{\Delta t}(\mathbf{d}_2 q_i^{n+1} - \mathbf{d}_2 q_i^n) \\ \frac{\partial^3 q}{\partial x^3} &\approx \theta \mathbf{d}_3 q_i^{n+1} + (1-\theta)\mathbf{d}_3 q_i^n \end{aligned} \tag{38}$$

Substituting Equations (38) into Equation (36) leads to

$$\frac{q_i^{n+1} - q_i^n}{\Delta t} = \frac{(h_i^n)^2}{3}\left(\frac{\mathbf{d}_2 q_i^{n+1} - \mathbf{d}_2 q_i^n}{\Delta t} + [\theta \mathbf{d}_3 q_i^{n+1} + (1-\theta)\mathbf{d}_3 q_i^n] u_i^n\right) \tag{39}$$

Rearranging leads to

$$\left[1 - \frac{h_i^n}{3}(\mathbf{d}_2 + \theta \Delta t u_i^n \mathbf{d}_3)\right] q_i^{n+1} = \left[1 - \frac{h_i^n}{3}(\mathbf{d}_2 - (1-\theta)\Delta t u_i^n \mathbf{d}_3)\right] q_i^n \tag{40}$$

The solution is sought in the form [34]

$$q_i^n = q_0^0 \exp[\omega(n\Delta t) + \mathrm{j}\mu(\mathrm{i}\Delta x)], \quad \mu \in [0, \pi] \tag{41}$$

Substituting Equation (41) into (37) leads to the following expressions:

$$\begin{aligned} \mathbf{d}_2 q_i^n &= \frac{2}{\Delta x^2}(\cos \mu \Delta x - 1) q_i^n \\ \mathbf{d}_3 q_i^n &= \frac{\mathrm{j}}{\Delta x^3}(\sin 2\mu \Delta x - 2 \sin \mu \Delta x) q_i^n \end{aligned} \tag{42}$$

where both quantities $(\cos \mu \Delta x - 1)$ and $(\sin 2\mu \Delta x - 2 \sin \mu \Delta x)$ are negative (note that μ belongs to the interval $[0, \pi]$). Substituting Equation (42) into (40) leads to an expression of the form

$$(1 - r_1 - \mathrm{j}\theta r_2) q_i^{n+1} = [1 - r_1 + \mathrm{j}(1-\theta) r_2] q_i^n \tag{43}$$

where r_1 and r_2 are given by

$$\begin{aligned} r_1 &= \frac{h_i^n}{3} \frac{2}{\Delta x^2}(\cos \mu \Delta x - 1) \\ r_2 &= \frac{h_i^n u_i^n}{3} \frac{\Delta t}{\Delta x^3}(\sin 2\mu \Delta x - 2 \sin \mu \Delta x) \end{aligned} \tag{44}$$

Note that both r_1 and r_2 are negative. The amplification factor A_N for the solution over the time step is

$$A_N \equiv \frac{q_i^{n+1}}{q_i^n} = \frac{1-r_1+\mathrm{j}(1-\theta)r_2}{1-r_1-\mathrm{j}\theta r_2} \tag{45}$$

The solution is stable if the modulus of A_N is smaller than or equal to unity. The modulus of A_N is

$$|A_N| = \left[\frac{(1-r_1)^2+[(1-\theta)r_2]^2}{(1-r_1)^2+(\theta r_2)^2}\right]^{1/2} \tag{46}$$

Clearly, the following properties hold regardless of the values of $\mu\Delta x$ and Δt:

$$\begin{aligned} |A_N| &< 1 \quad \text{for } \theta > \tfrac{1}{2} \\ |A_N| &= 1 \quad \text{for } \theta = \tfrac{1}{2} \\ |A_N| &> 1 \quad \text{for } \theta < \tfrac{1}{2} \end{aligned} \tag{47}$$

In other words, the discretization is unconditionally unstable for $\theta < \frac{1}{2}$ and unconditionally stable for $\theta \geqslant \frac{1}{2}$. Using $\theta = \frac{1}{2}$ allows the amplitude of the numerical solution to be preserved, which corresponds to the behaviour of the analytical solution outlined in Section 2. Increasing the computational time step causes an increase in the magnitude of r_2, thus increasing the unstable character of the scheme for $\theta < \frac{1}{2}$ and increasing the numerical damping for $\theta > \frac{1}{2}$. The value $\theta = \frac{1}{2}$ has been adopted in the application examples shown in Section 4.

The stability analysis above is extended to the predictor–corrector framework presented in Section 3.1 as follows. The predictor–corrector procedure can be summarized by the following sequence of numerical operators:

$$\mathbf{U}^{n+1} = \mathbf{CBPU}^n \tag{48}$$

where **C**, **B** and **P** are the corrector, dispersion and predictor operators, respectively. Reasoning by recurrence, Equation (48) can be rewritten as

$$\mathbf{U}^{n+1} = (\mathbf{CBP})^n \mathbf{U}^0 = \mathbf{C}(\mathbf{BPC})^{n-1}\mathbf{BPU}^0 \tag{49}$$

where $\mathbf{U}^0$ is the initial condition. The numerical solution is stable if the sequence (**BPC**) yields a stable solution. Note that the classical MUSCL scheme [35] can be described by the following sequence:

$$\mathbf{U}^{n+1} = \mathbf{CPU}^n \tag{50}$$

Again, reasoning by recurrence, Equation (50) can be rewritten as

$$\mathbf{U}^{n+1} = (\mathbf{CP})^n \mathbf{U}^0 = \mathbf{C}(\mathbf{PC})^{n-1}\mathbf{PU}^0 \tag{51}$$

The sequence (**CP**), and therefore the sequence (**PC**), is known to yield a stable solution provided that the following Courant–Friedrichs–Lewy (CFL) condition is satisfied:

$$\mathrm{CFL} = \frac{\Delta t}{\Delta x_i} \max(|u_i^n - c_i^n|, |u_i^n + c_i^n|) \leqslant 1 \quad \forall i \tag{52}$$

Therefore, the sequence (**CBP**) is stable provided that both the MUSCL scheme and the proposed discretization for the dispersion terms are stable. In other words, stability is ensured if the CFL condition (52) and the stability condition (47) are satisfied simultaneously.

3.4. Modified MUSCL reconstruction

The present section focuses on the solution of the hyperbolic part of the equation. It is reminded that the predictor step consists in computing a first version of the fluxes using the 'guessed' values of the flow variables at the interfaces between the computational cells. Such values were guessed using the MUSCL reconstruction:

$$\begin{aligned}\mathbf{U}_{i,\mathrm{L}}^{n} &= \widetilde{\mathbf{U}}_{i}^{n}(x_{i+1/2})\\ \mathbf{U}_{i,\mathrm{R}}^{n} &= \widetilde{\mathbf{U}}_{i}^{n}(x_{i-1/2})\end{aligned} \tag{53}$$

where $\widetilde{\mathbf{U}}_{i}^{n}(x)$ is the reconstructed profile function within the cell i at the time level n. In the original version of the scheme [1] the reconstruction function was given by the classical MUSCL reconstruction:

$$\widetilde{\mathbf{U}}_{i}^{n}(x)=\mathbf{U}_{i}^{n}+(x-x_i)\delta\mathbf{U}_{x_i}^{n} \tag{54}$$

The classical option consists in approaching the slope $\delta\mathbf{U}_{x_i}^{n}$ of $\mathbf{U}$ using the following first approximation $\delta\mathbf{U}_{x_i}^{(1)^n}$ (given here for an irregular grid):

$$\begin{aligned}\delta\mathbf{U}_{x_i}^{(1)^n} =& \frac{\Delta x_{i+1/2}}{(\Delta x_{i+1/2}+\Delta x_{i-1/2})\Delta x_{i-1/2}}(\mathbf{U}_{i+1}^{n}-\mathbf{U}_{i}^{n})\\ &+\frac{\Delta x_{i-1/2}}{(\Delta x_{i+1/2}+\Delta x_{i-1/2})\Delta x_{i+1/2}}(\mathbf{U}_{i}^{n}-\mathbf{U}_{i-1}^{n})\end{aligned} \tag{55}$$

where $\Delta x_{i-1/2}=(x_i-x_{i-1})=(\Delta x_{i-1}+\Delta x_i)/2$ is the distance between the gravity centres of the cells i and $i-1$. Note that for a regular grid with constant cell width Δx Equation (55) simplifies into

$$\delta\mathbf{U}_{x_i}^{(1)^n} = \frac{1}{2\Delta x}(\mathbf{U}_{i+1}^{n}-\mathbf{U}_{i-1}^{n}) \tag{56}$$

A fourth-order Taylor series expansion in $\mathbf{U}$ yields the following truncation error:

$$\begin{aligned}\delta\mathbf{U}_{x_i}^{(1)^n} =& \frac{\partial\mathbf{U}}{\partial x}+\frac{\Delta x_{i-1/2}\Delta x_{i+1/2}}{6}\frac{\partial^3\mathbf{U}}{\partial x^3}\\ &+\frac{\Delta x_{i-1/2}\Delta x_{i+1/2}(\Delta x_{i+1/2}-\Delta x_{i-1/2})}{6}\frac{\partial^4\mathbf{U}}{\partial x^4}+\mathrm{HOT}\end{aligned} \tag{57}$$

Consequently, discretization (57) is second-order accurate in $\mathbf{U}$ when the grid is irregular and third order in $\mathbf{U}$ when the grid is regular.

DOI: 10.1002/fld

Note that Equation (55) could also be applied to the cells $i-2$, i and $i+2$ instead of the cells $i-1$, i and $i+1$, leading to a second possible slope estimate $\delta \mathbf{U}_{x_i}^{(2)^n}$:

$$\begin{aligned}\delta \mathbf{U}_{x_i}^{(2)^n} = {} & \frac{\Delta x_{i+1/2}+\Delta x_{i+3/2}}{(\Delta x_{i-3/2}+\Delta x_{i-1/2})\sum_{k=-1}^{2}\Delta x_{i-1/2+k}}(\mathbf{U}_{i+2}^{n}-\mathbf{U}_{i}^{n}) \\ & +\frac{\Delta x_{i-3/2}+\Delta x_{i-1/2}}{(\Delta x_{i+1/2}+\Delta x_{i+3/2})\sum_{k=-1}^{2}\Delta x_{i-1/2+k}}(\mathbf{U}_{i}^{n}-\mathbf{U}_{i-2}^{n})\end{aligned} \tag{58}$$

the fourth-order Taylor series expansion of which is

$$\begin{aligned}\delta \mathbf{U}_{x_i}^{(2)^n} = {} & \frac{\partial \mathbf{U}}{\partial x}+\frac{(\Delta x_{i-3/2}+\Delta x_{i-1/2})(\Delta x_{i+1/2}+\Delta x_{i+3/2})}{6}\frac{\partial^3 \mathbf{U}}{\partial x^3} \\ & +\frac{(\Delta x_{i-3/2}+\Delta x_{i-1/2})(\Delta x_{i+1/2}+\Delta x_{i+3/2})}{6} \\ & \times(-\Delta x_{i-3/2}-\Delta x_{i-1/2}+\Delta x_{i+1/2}+\Delta x_{i+3/2})\frac{\partial^4 \mathbf{U}}{\partial x^4}+\mathrm{HOT}\end{aligned} \tag{59}$$

The third-order derivatives can be eliminated by combining Equations (55) and (57) into a third estimate $\delta \mathbf{U}_{x_i}^{(3)^n}$ given by

$$\begin{aligned}\delta \mathbf{U}_{x_i}^{(3)^n} &= \frac{a^{(1)}\mathbf{U}_{x_i}^{(1)^n}-a^{(2)}\mathbf{U}_{x_i}^{(2)^n}}{a^{(1)}-a^{(2)}} \\ a^{(1)} &= (\Delta x_{i-3/2}+\Delta x_{i-1/2})(\Delta x_{i+1/2}+\Delta x_{i+3/2}) \\ a^{(2)} &= \Delta x_{i-1/2}\Delta x_{i+1/2}\end{aligned} \tag{60}$$

Equation (60) is third-order accurate in $\mathbf{U}$ on irregular grids and fourth-order accurate on regular grids. Note that this higher-order estimate of the slope does not mean that the resulting MUSCL4 scheme is fourth-order accurate. Indeed, the proposed modification affects only the estimate of the slope in Equation (54) and not the order of the reconstruction itself. In other words, the order of the truncation error remains the same in the proposed MUSCL4 scheme as in the original scheme, but its amplitude is smaller.

To prevent the appearance of oscillations near steep gradients, a limiter should be applied. Three limiting options are investigated in the application example of the solitary wave: the classical minmod limiter presented in [36], the monotonized central-difference limiter of Van Leer, also presented in [36], and the shock detecting limiter by Krivodonova *et al.* [37].

4. APPLICATION EXAMPLES

Three different applications of flow in a frictionless horizontal channel involving free-surface undulations that can be represented by the dispersive terms of the Boussinesq equations are shown. First, the example of the propagation of a solitary wave is used to illustrate the ability of the proposed scheme to reproduce an analytical solution of the equations. Then, the development of an undular bore is presented, both from a theoretical point of view and by means of laboratory experiments.

For all these applications, boundary conditions need to be applied. This is done using the ghost cell technique [38, 39].

4.1. Propagation of a solitary wave

In order to assess the performance of the proposed scheme, numerical experiments of propagation of a solitary wave were performed. The initial water profile was taken from Peregrine [40]

$$\eta(x,t=0)=a_0h_0\,\mathrm{sech}^2\left(\tfrac{1}{2}\sqrt{3a_0}(x-x_0)\right) \tag{61}$$

where η is the wave height above the undisturbed water depth h_0, i.e. $h=h_0+\eta$. The solitary wave amplitude is a_0, and x_0 is the initial abscissa of the wave crest. The wave has a constant initial celerity

$$V_0=\sqrt{gh_0}(1+a_0/2) \tag{62}$$

Substituting Equations (61) and (62) into the continuity equation allows the initial velocity profile to be defined as

$$u(x,t=0)=V_0\frac{\eta(x,t=0)}{h_0+\eta(x,t=0)} \tag{63}$$

As the solitary wave propagates without changing its shape, the analytical solution for the water profile is simply given by

$$\eta(x,t)=a_0h_0\,\mathrm{sech}^2\left(\tfrac{1}{2}\sqrt{3a_0}(V_0t-x_0)\right) \tag{64}$$

The numerical values of the parameters are given in Table I. Figure 3 shows the results computed using the semi-implicit scheme with the fourth-order MUSCL variable reconstruction (hereafter denoted as MUSCL4 scheme) on a refined grid ($\Delta x=0.05\,\mathrm{m}$). The initial wave is shown, and the computed solution after 18 s, matching perfectly the analytical solution.

The effect of the various reconstructions is illustrated in Figure 4. The solutions are computed using a cell size $\Delta x=0.5\,\mathrm{m}$, with $\theta=0.5$ and CFL$=0.9$. The Godunov scheme can be seen to yield an unacceptable damping of the wave. The MUSCL scheme with the minmod limiter yields better results; however, the wave remains strongly damped. The proposed MUSCL4 scheme allows the

Table I. Propagation of a solitary wave. Parameters of the test case.

Symbol	Meaning	Value
a_0	Amplitude of the solitary wave	0.1 m
CFL	Value of the Courant–Friedrichs–Lewy number	0.1, 0.5, 0.9
g	Gravitational acceleration	$9.81\,\mathrm{m}^2\,\mathrm{s}^{-1}$
h_0	Initial water depth	1 m
x_0	Initial abscissa of the crest of the wave	20 m
Δx	Computational cell width	0.05 m, 0.5 m
θ	Implicitation parameter	0.0, 0.5, 0.6, 1.0

DOI: 10.1002/fld

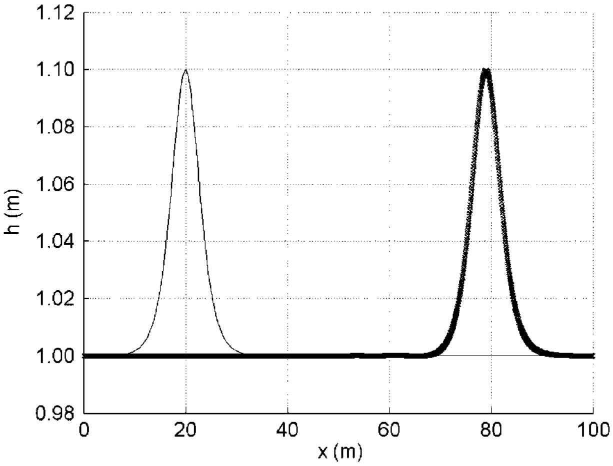

Figure 3. Initial condition (wave centred at $x = 20\,\mathrm{m}$) and comparison between the numerical solution (dots) for CFL$=0.9$, $\Delta x = 0.05\,\mathrm{m}$ and $\theta = 0.5$ after 18 s and the analytical solution (continuous line).

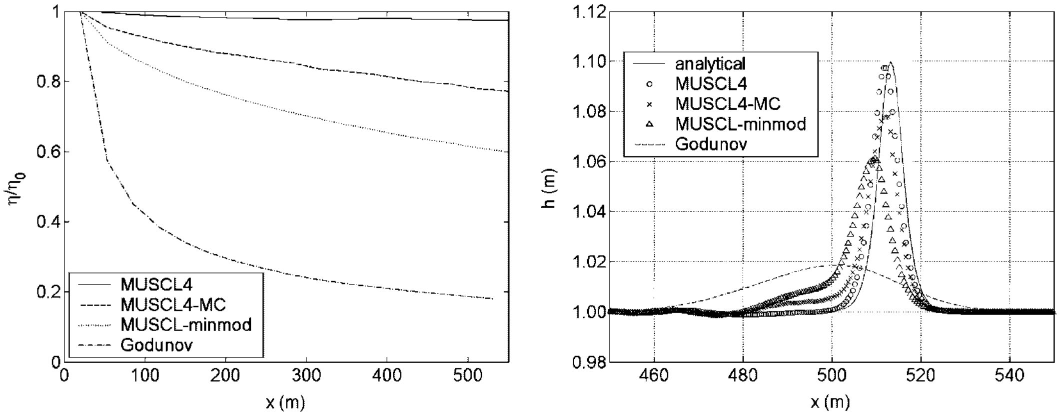

Figure 4. Influence of the numerical scheme on solution accuracy. Wave amplitude as a function of distance (left) and water depth profile at $t = 150\,\mathrm{s}$ (right). Solutions obtained for CFL$=0.9$, $\Delta x = 0.5\,\mathrm{m}$ and $\theta = 0.5$.

analytical solution to be better reproduced. Figure 4 shows the results obtained using the scheme in conjunction with the monotonized central-difference limiter of Van Leer (MUSCL4-MC in the figure). A last option consists in applying the limiter only in the vicinity of steep gradients, following a shock detection procedure [37] (results labelled MUSCL4 in the figure). In the present case, it unexpectedly appears that this option corresponds to not applying the limiter at all, as the solitary wave does not induce any steep gradient, and thus no shock was detected. Therefore, the solution is almost not damped and the characteristics of the solitary wave are well preserved.

As outlined in the stability analysis, when $\theta = 0.5$ the numerical solution is stable and the amplification factor is equal to unity, regardless of the time step. This is illustrated in Figure 5,

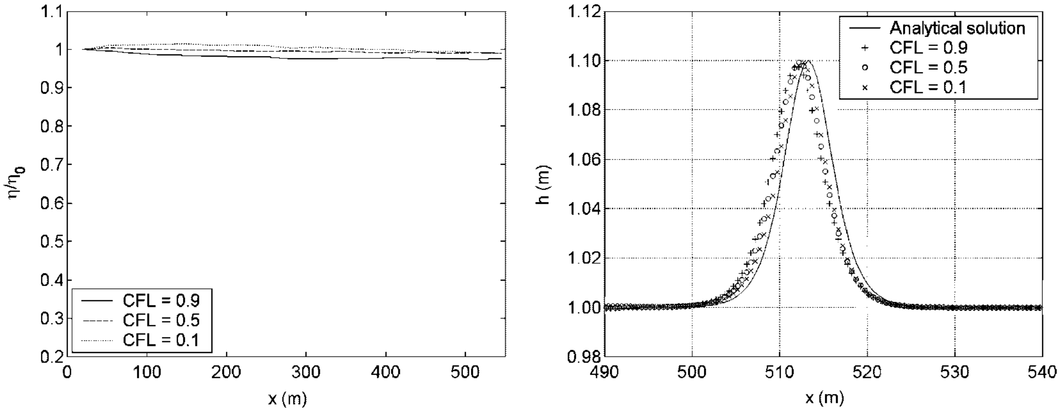

Figure 5. Influence of the time step on the results computed with the MUSCL4 scheme, $\theta = 0.5$: wave amplitude as a function of distance (left) and water depth profile at $t = 150\,\mathrm{s}$ (right). Solutions obtained for $\Delta x = 0.05\,\mathrm{m}$ and $\theta = 0.5$.

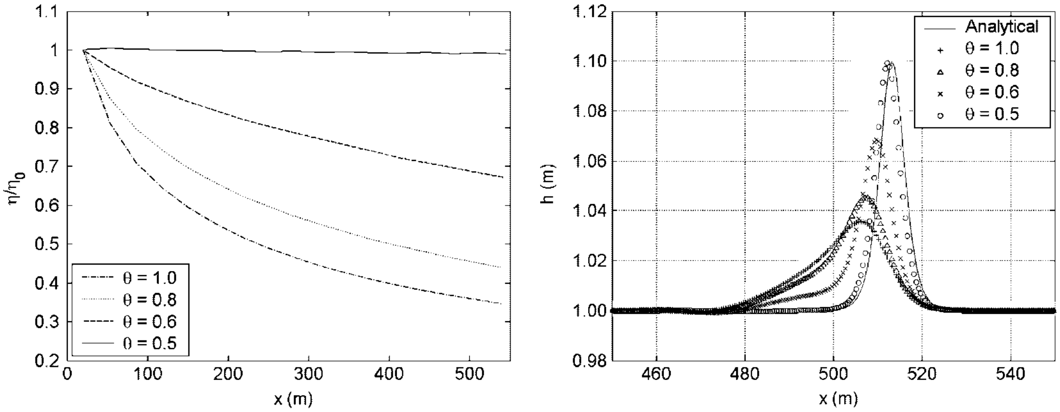

Figure 6. Influence of θ on the results computed with the MUSCL4 scheme, CFL $= 0.5$: wave amplitude as a function of distance (left) and water depth profile at $t = 150\,\mathrm{s}$ (right). Solutions obtained for CFL $= 0.9$ and $\Delta x = 0.5\,\mathrm{m}$.

comparing results computed with the MUSCL4 scheme, with $\Delta x = 0.5\,\mathrm{m}$ and $\theta = 0.5$, and using three different CFL numbers. The wave amplitude is well preserved: the computed amplification factor η/η_0 is close to 1. The delay of the wave is reduced for smaller time steps (CFL $= 0.1$).

Results for various values of θ are presented in Figure 6. Using a fully implicit scheme ($\theta = 1$) has a strong negative effect on the amplification factor. Even for $\theta = 0.6$, the damping is very strong. The lag between the numerical and the analytical solution is seen to increase with θ.

Finally, the behaviour of the scheme is investigated for $\theta = 0$, which from the stability analysis in Section 3.2 should be expected to yield an unstable solution. This is illustrated in Figure 7, where the computed results rapidly diverge from the analytical solution, with important over- and undershoots.

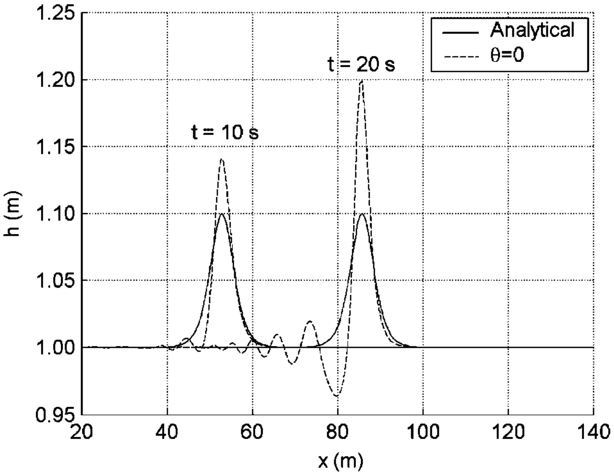

Figure 7. Instability of the numerical scheme for $\theta = 0$. Water depth computed at $t = 10$ and 20 s. Numerical solution obtained for CFL = 0.9 and $\Delta x = 0.5$ m.

4.2. Development of an undular bore

According to the shallow-water theory, a long wave steepens as it travels and may eventually form a bore [41]. In most cases, such a bore develops into a turbulent zone of breaking water, the length of which is about 6 times the water depth. However, if the bore is weak, a train of long, almost periodic waves develops. From a physical point of view, the growth of an undular bore is due to the free-surface curvature, inducing extra horizontal pressure gradients as a consequence of the vertical acceleration of the water [1, 2]. This was illustrated by Peregrine [2], showing how a smooth wave steepens when considering only the classical shallow-water equations, and how undulations grow at the head of the bore when the Boussinesq equations accounting for weak non-hydrostaticity are used, while such a phenomenon cannot be reproduced using the shallow-water equations. The initial wave profile used by Peregrine was

$$\eta = \frac{1}{g}\left(u\sqrt{gh_0} + \frac{1}{4}u^2\right) \tag{65}$$

$$u = \tfrac{1}{2}u_0\sqrt{gh_0}[1 - \tanh(x/a)] \tag{66}$$

with the water depth $h = h_0 + \eta$, h_0 being the undisturbed initial water depth, u_0 the velocity of the incoming wave and a a parameter describing the shape of the incoming wave (a smaller value of a gives a steeper initial profile).

Computations of the propagation of such a wave and its development into an undular bore are shown in Figure 8. Table II summarizes the parameters of the simulation. The computations are run with $\Delta x = 0.2$ m using three different schemes. First, the classical shallow water is used, solved by a Roe-type finite-volume scheme [30]. Then, the finite-difference scheme by Peregrine [2] is used to solve the Boussinesq equations (1) and finally the hybrid finite-volume scheme with MUSCL4 reconstruction proposed in the present paper, with $\theta = 0.5$ and CFL = 0.9. The solution of the shallow-water equations leads to a progressive steepening of the bore without any undulation, while

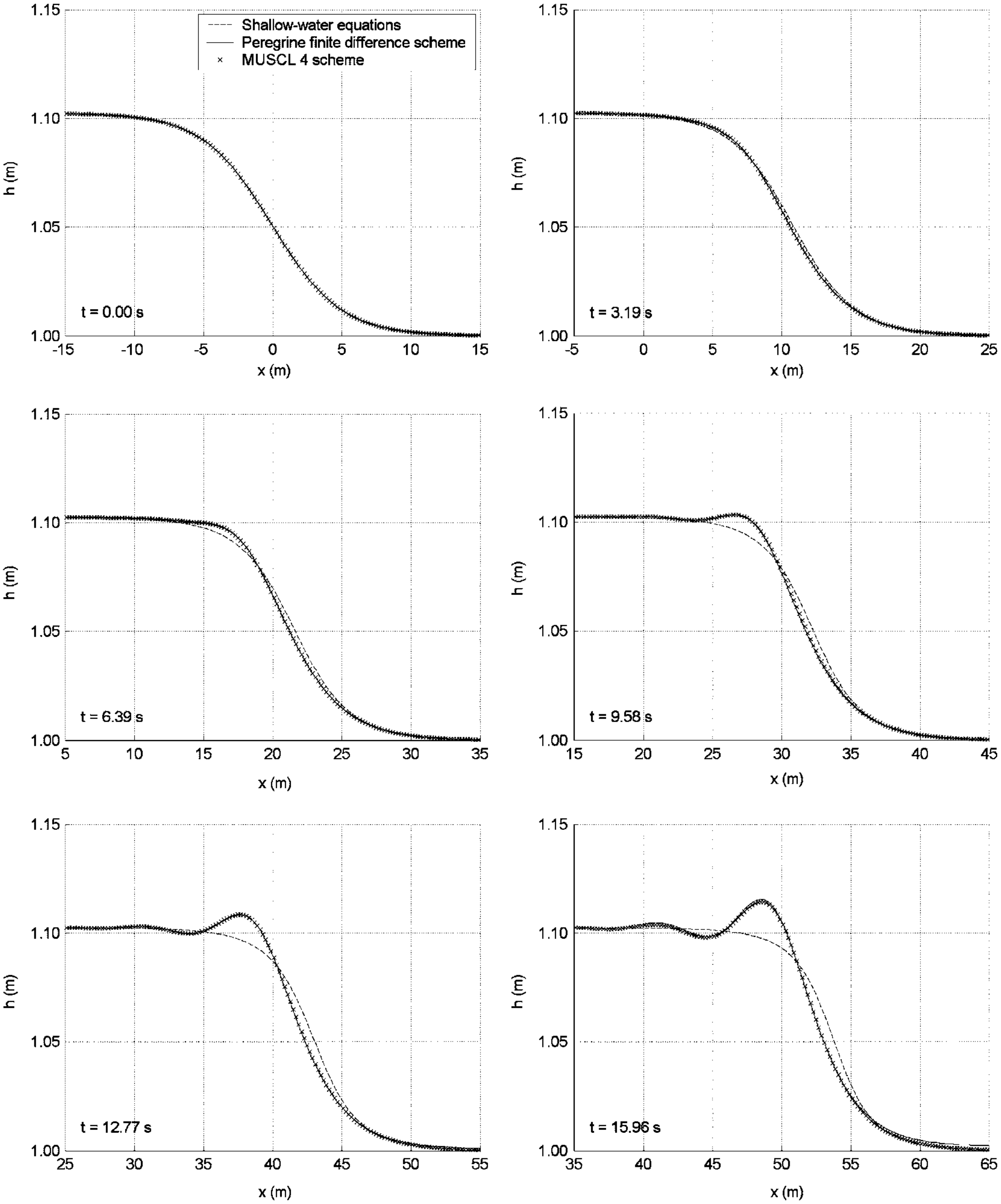

Figure 8. Development of an undular bore computed with the shallow-water equations and with the Boussinesq equations (Peregrine finite-difference scheme [9] and MUSCL4 scheme).

Table II. Development of an undular bore. Parameters of the numerical test case.

Symbol	Meaning	Value
a	Characteristic length of the bore	5 m
CFL	Value of the Courant–Friedrichs–Lewy number	0.9
g	Gravitational acceleration	$9.81\,\mathrm{m}^2\,\mathrm{s}^{-1}$
h_0	Undisturbed, initial water depth	1 m
u_0	Velocity behind the bore	$0.1\,\mathrm{m\,s}^{-1}$
Δx	Computational cell width	0.2 m
θ	Implicitation parameter	0.5

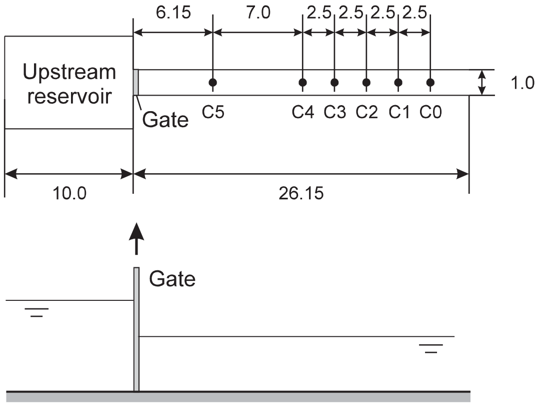

Figure 9. Experimental set-up. Dimensions in metres.

the Boussinesq equations solved by Peregrine's method and the proposed numerical technique allow the growth of the undulations at the head of the bore to be reproduced.

4.3. *Experimental validation*

Undular bores were reproduced experimentally by Favre [3] who showed that undular bores form when the ratio of the change in level to the initial water depth is smaller than 0.28. Similar experiments were conducted by Soares-Frazão and Zech [1]. The experimental data are used here to validate the proposed MUSCL4 scheme. The experimental set-up, located in the laboratory of the Civil and Environmental Engineering Department of the University of Louvain (Université catholique de Louvain—UCL), is sketched in Figure 9. The channel bed is horizontal, and a gate separates the upstream reservoir from the channel. The water is initially at rest in both regions. When the gate is opened rapidly, a bore forms and travels in the downstream channel (Figure 10). Note that the gate is not open in full but raised so that its bottom level remains below the initial level in the upstream part of the channel. This allows the flow cross-sectional area and the upstream hydraulic head, thus the discharge, to be maintained at a constant value for a sufficiently long time. Water-level gauges ($C0$–$C5$) were placed in the channel to record the time evolution of the water level. The characteristics of the experiments are summarized in Table III.

The measurements are compared with the numerical results computed with the MUSCL4 scheme in Figure 11. The results obtained by using the hybrid finite-volume scheme of [1] are also

DOI: 10.1002/fld

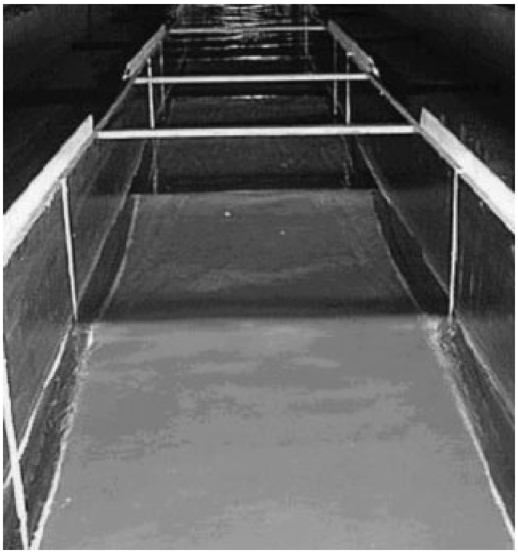

Figure 10. Undular bore experiment. View from the upstream end of the canal.

Table III. Development of an undular bore. Parameters of the experiments.

Symbol	Meaning	Value
CFL	Value of the Courant–Friedrichs–Lewy number	0.9
g	Gravitational acceleration	$9.81\,\mathrm{m^2\,s^{-1}}$
h_0	Undisturbed, initial water depth	$0.251\,\mathrm{m}$
q_g	Unit discharge at the gate	$0.059\,\mathrm{m\,s^{-1}}$
Δx	Computational cell width	$0.05\,\mathrm{m}$
θ	Implicitation parameter	0.5

indicated. The significant improvement in the computed results with the MUSCL4 scheme can be clearly observed: the attenuation of the wave train occurs slower than with the former scheme. The growth of the first wave is more rapid in the experiment than in both numerical schemes. At gauge $C5$, the closest to the gate, the actual wave has already reached its maximum amplitude (about 0.31 m), while the numerical waves still grow. When reaching gauge $C3$, the wave simulated with the MUSCL4 scheme has grown to the correct amplitude, while the amplitude of the wave simulated with the former scheme is too small. Table IV gives the experimental and numerical values of the ratio of the first wave amplitude a_0 to the average upstream water depth h_0 and the ratio of the wavelength l_0 to h_0, as measured when the wave passes at gauge $G1$.

It should be noted that the MUSCL4 reconstruction yields better results than the classical MUSCL reconstruction in the present situation where the initial profile is continuous and remains so at later times. Numerical experiments, not reported here for the sake of conciseness, have shown that when the classical shallow-water equations are to be solved with the possible development of discontinuous solutions, the MUSCL scheme gives better results than the MUSCL4 reconstruction owing to its smaller stencil. The well-known fact that slope limiting applied to schemes with large

DOI: 10.1002/fld

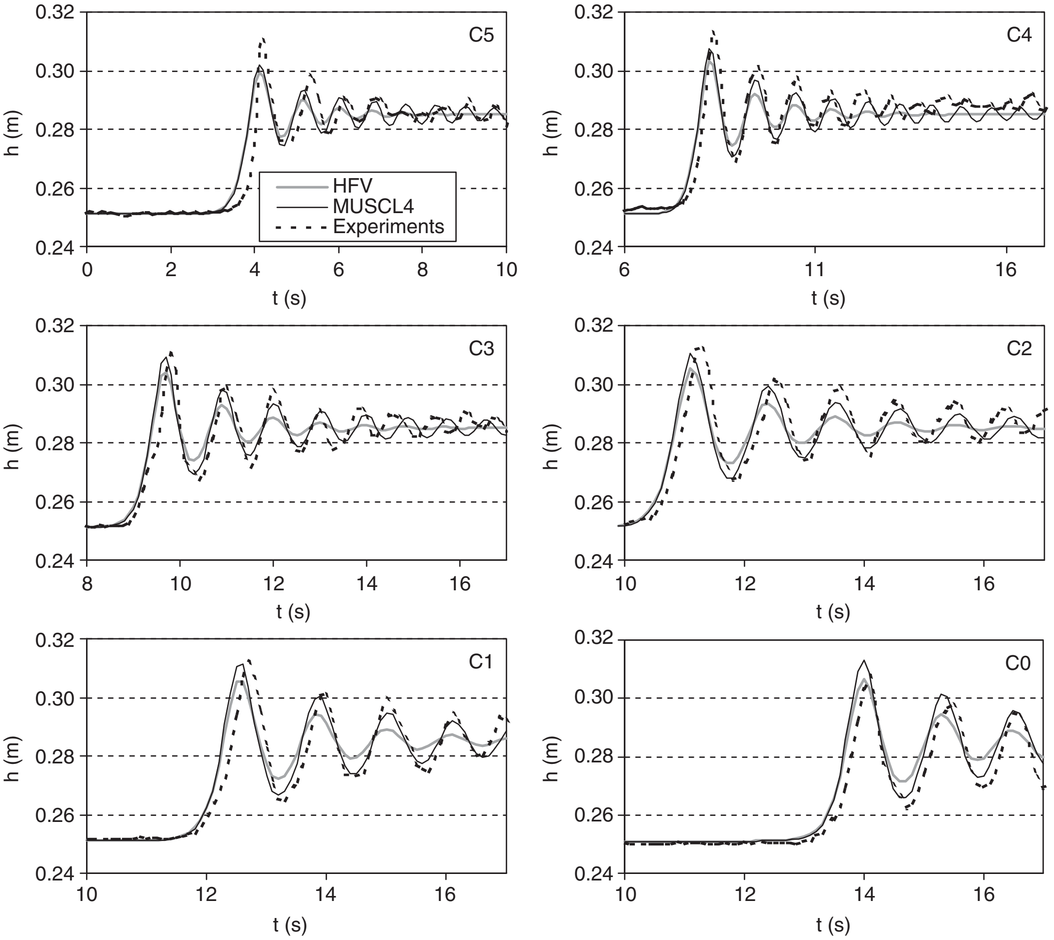

Figure 11. Experimental and computed water levels at the five gauging stations. Numerical results obtained using the hybrid finite volume scheme (HFV) and the proposed scheme (MUSCL4).

Table IV. Development of an undular bore. Characteristics of the bore.

Symbol	Meaning	Value at gauge $C1$
a_0/h_0	Ratio of the first wave amplitude to the initial water depth	0.245 (experimental) 0.217 (MUSCL scheme) 0.247 (MUSCL4 scheme)
l_0/h_0	Ratio of the first wave length to the initial water depth	8.864 (experimental) 8.903 (MUSCL scheme) 9.189 (MUSCL4 scheme)

stencils may lead to smoother fronts is usually solved by devising several slope estimates and using the steepest one that preserves the monotonicity of the profile (see [42] for an example). However, such an approach does not need to be applied in the present applications, where smooth profiles are dealt with.

5. CONCLUSIONS

A new semi-implicit hybrid discretization (finite volumes/finite differences) is proposed to solve the Boussinesq equations, for the simulation of flows presenting weak deviations from the classical hydrostatic shallow-water theory. The scheme features an improved treatment of the hyperbolic terms, combining Riemann solvers and semi-implicitation for the momentum equation, and a discretization of the dispersive terms that is less sensitive to the computational time step than a previously proposed hybrid scheme. Indeed, a stability analysis of the proposed scheme shows that for an implicitation factor $\theta = 0.5$, the solution is neither amplified nor damped.

A higher-order formula is proposed for the estimate of the slope in the MUSCL reconstruction in order to increase the accuracy of the numerical results. Comparisons with results obtained using the classical MUSCL approach illustrate the performances of this new scheme. Numerical experiments show the ability of the proposed scheme to simulate the propagation of a solitary wave and the growth of an undular bore. The example of the solitary wave, where the wave propagates without deforming, shows that the proposed scheme is able to reproduce the analytical solution. The results obtained for the growth of an undular bore are compared successfully with the results given by Peregrine's finite-difference scheme.

Finally, a comparison with an experimental test case was presented, in which the proposed scheme reproduces the measurements with a good agreement. In particular, a comparison with past studies highlights the efficiency of the new discretization of the dispersive terms and of the new variable reconstruction scheme.

REFERENCES

1. Soares-Frazão S, Zech Y. Undular bores and secondary waves—experiments and hybrid finite-volume modelling. *Journal of Hydraulic Research* 2002; **40**(1):33–43.
2. Peregrine DH. Calculations of the development of an undular bore. *Journal of Fluid Mechanics* 1966; **25**(3): 321–330.
3. Favre H. *Ondes de Translation*. Dunod: Paris, 1935.
4. Lemoine R. Sur les ondes positives de translation et sur le ressaut ondulé de faible amplitude. *La Houille Blanche* 1948; **2**(March–April):183.
5. Nadiga BT, Margolin LG, Smolarkiewicz PK. Different approximations of shallow fluid flow over an obstacle. *Physics of Fluids* 1996; **8**(8):2066–2077.
6. Apel JP. A new analytical model for internal solitons in the ocean. *Journal of Physical Oceanography* 2003; **33**(11):2247–2269.
7. El GA, Grimshaw RHJ, Smyth NF. Unsteady undular bores in fully nonlinear shallow-water theory. *Physics of Fluids* 2006; **18**(2):027104 (17 pages).
8. Cunge JA. Discussion of 'Undular bores and secondary waves—experiments and hybrid finite-volume modelling'. *Journal of Hydraulic Research* 2003; **41**(5):557–559.
9. Benet F, Cunge JA. Analysis of experiments on secondary undulations caused by surge waves in trapezoidal channels. *Journal of Hydraulic Research* 1971; **9**(1):11–32.
10. Treske A. Undular bores (Favre Waves) in open channels—experimental studies. *Journal of Hydraulic Research* 1994; **32**(3):355–370.

11. Ponsy J, Carbonnell M. Étude photogrammétrique d'intumescences dans le canal d'amenée de l'usine d'Oraison (Basses Alpes) (in French)—photogrammetric study of waves in the power canal of Oraison (Basses Alpes, France) hydropower station. *Journal de la Société Française de Photogrammétrie* 1966; **22**:18–28.
12. Marche C, Beauchemin P, El Kayloubi A. Etude numérique et expérimentale des ondes secondaires de Favre consécutives à la rupture d'un barrage. *Canadian Journal of Civil Engineering* 1995; **22**:793–801.
13. Preissmann A, Cunge JA. Low amplitude undulating hydraulic jump in trapezoidal canals. *Journal of Hydraulic Research* 1967; **5**(4):263–279.
14. Prüser HH, Zielke W. Undular bores (Favre Waves) in open channels—theory and numerical simulation. *Journal of Hydraulic Research* 1994; **32**(3):337–354.
15. Wei G, Kirby JT. Time-dependent numerical code for extended Boussinesq equations. *Journal of Waterway*, *Port*, *Coastal and Ocean Engineering* 1995; **121**(5):251–261.
16. Bratsos AG, Famelis ITh, Prospathopoulos AM. A parametric finite-difference method for shallow sea waves. *International Journal for Numerical Methods in Fluids* 2007; **53**(1):129–147.
17. Erduran KS, Ilic S, Kutija V. Hybrid finite-volume finite-difference scheme for the solution of Boussinesq equations. *International Journal for Numerical Methods in Fluids* 2005; **49**(11):1213–1232.
18. Erduran KS. Further application of hybrid solution to another form of Boussinesq equations and comparisons. *International Journal for Numerical Methods in Fluids* 2007; **53**(5):827–849.
19. Cienfuegos R, Barthélemy E, Bonneton P. A fourth-order compact finite volume scheme for fully nonlinear and weakly dispersive Boussinesq-type equations. Part I: model development and analysis. *International Journal for Numerical Methods in Fluids* 2006; **51**(11):1217–1253.
20. Stansby PK. Solitary wave run up and overtopping by a semi-implicit finite-volume shallow-water Boussinesq model. *Journal of Hydraulic Research* 2003; **41**(6):639–647.
21. Walkley M, Berzins M. A finite element method for the one-dimensional extended Boussinesq equations. *International Journal for Numerical Methods in Fluids* 1999; **29**:143–157.
22. Woo SB, Liu PLF. A Petrov–Galerkin finite-element model for one-dimensional fully non-linear and weakly dispersive wave propagation. *International Journal for Numerical Methods in Fluids* 2001; **37**:541–575.
23. Antunes Do Carmo JS, Seabra Santos FJ, Barthélemy E. Surface waves propagation in shallow water: a finite element model. *International Journal for Numerical Methods in Fluids* 1993; **16**(6):447–459.
24. Walters RA. A semi-implicit finite element model for non-hydrostatic (dispersive) surface waves. *International Journal for Numerical Methods in Fluids* 2005; **49**(7):721–737.
25. Whitham GB. *Linear and Nonlinear Waves*. Wiley: New York, 1974.
26. Marchant TR. Solitary wave interaction for the extended BBM equation. *Proceedings of the Royal Society of London* 2000; **456**:433–453.
27. Luo Z, Liu R. Mixed finite-element analysis and numerical solitary solution for the RLW equation. *SIAM Journal on Numerical Analysis* 1998; **36**(1):89–104.
28. Sanders BF, Katopodes ND, Boyd JP. Spectral modeling of nonlinear dispersive waves. *Journal of Hydraulic Engineering* 1998; **124**(1):2–12.
29. Vichnetvetsky R, Bowles JB. *Fourier Analysis of Numerical Approximations of Hyperbolic Equations*. SIAM Studies in Applied Mathematics: Philadelphia, PA, 1982.
30. Soares-Frazão S, Zech Y. Dam-break in channels with 90° bend. *Journal of Hydraulic Engineering* 2002; **128**(12):956–968.
31. Hirsch C. *Numerical Computation of Internal and External Flows*. Wiley: U.K., 1997.
32. Strang G. On the construction and comparison of difference schemes. *SIAM Journal on Numerical Analysis* 1968; **5**:506–517.
33. Crandall M, Majda A. The method of fractional steps for conservation laws. *Numerische Mathematik* 1980; **34**:285–314.
34. Richtmyer RD, Morton KW. *Difference Methods for Initial-value Problems*. Interscience: New York, 1967.
35. Alcrudo F, Garcia-Navarro P. A high resolution Godunov-type scheme in finite volumes for the 2D shallow-water equations. *International Journal for Numerical Methods in Fluids* 1993; **16**:489–505.
36. LeVeque RJ. *Finite Volume Methods for Conservation Laws.* Cambridge University Press: Cambridge, 2002.
37. Krivodonova L, Xin J, Remacle JF, Chevaugeon N, Flaherty JE. Shock detection and limiting with discontinuous Galerkin methods for hyperbolic conservation laws. *Applied Numerical Mathematics* 2004; **48**:323–338.
38. Guinot V. Boundary condition treatment in 2×2 systems of propagation equations. *International Journal for Numerical Methods in Engineering* 1998; **42**:647–666.
39. Guinot V. The discontinuous profile method for simulating two-phase flow in pipes using the single-component approximation. *International Journal for Numerical Methods in Fluids* 2001; **37**:341–359.

40. Peregrine DH. Long waves on a beach. *Journal of Fluid Mechanics* 1967; **27**(5):815–827.
41. Stoker JJR. *Water Waves*. Interscience: New York, 1957.
42. Colella P, Woodward PR. The piecewise parabolic method (PPM) for gas-dynamical simulations. *Journal of Computational Physics* 1984; **54**:174–201.